decoupling between the Kaapvaal crust and its present mantle root. It follows that Archean crust can couple to Archean mantle at more than one time before the birth of the tectosphere.

Our data place a maximum age of 3.09 Ga on the time of crust-root coupling, given that this is the last recognized time of voluminous granite magmatism in the Vredefort section. Magmatic intraplating and/or impact related effects at the crust-mantle boundary have caused local granulite-facies metamorphism at 2.7, 2.0, and 1.0 Ga (24, 25), but these thermal events in the Mesoarchean crust as a whole have been minor relative to the events at ~3.1 Ga. The presence of Neoarchean dolerite dykes (16) also argues against elevated (>400°C) crustal temperatures after this time. A lower limit of 3.07 Ga for tectosphere birth is derived from the age of basal volcanic and sedimentary rocks of the Witwatersrand Basin, part of a passive continental margin sequence deposited on the stabilized crystalline crust (1, 7). On the basis of these upper and lower limits, we place the age of permanent crust-mantle coupling (tectosphere initiation) beneath the central Kaapvaal crust at 3.08 ± 0.01 Ga.

Given our 3.08 Ga age for Kaapvaal tectosphere birth, there is a ~120 million year gap between the 3.2 Ga assembly of the Mesoarchean crust of the craton (7) and its coupling to the mantle root. This indicates an allochthonous relation between the crust and mantle root, consistent with continental genesis models that portray crust and mantle lithosphere as components generated in different tectonic settings before unification (e.g., 3, 5). A model of root formation by accretion of oceanic lithosphere plates (5) is supported by recent Re-Os dating that reports about 3 Ga eclogitized oceanic crust beneath much of the craton (26). Moreover, the discovery of 2.86 ± 0.06 Ga sulphide inclusions in eclogitic diamonds beneath the center of the craton indicates root thickening to >150 km (the approximate depth to diamond stability field) by this time (27). Thus, the construction of the tectosphere took place within roughly 0.2 Gy of tectosphere initiation.

Our integrated mapping and high-precision geochronology of the deep Kaapvaal crust demonstrates that tectosphere birth can post-date the age of its crust and mantle components by several hundred million years, with crust assembly preceding subduction-driven mantle root construction by at least 0.12 Ga. A similar rate and process of tectosphere genesis later in the Archean can be inferred from limited data for 2 of the 10 other tectosphere fragments; namely the Superior craton of North America (22, 28) and the Siberian craton (29). Further lower crust and mantle root geochronology will test whether indeed all such ancient continental plates were created equally.

References and Notes

1. G. Brandl, M. J. de Wit, in *Greenstone Belts*, M. J. de Wit, L. D. Ashwal, Eds. (Oxford Monographs on Geology and Geophysics, Oxford, UK, 1997), vol. 35, chap. 5.8, pp. 581–607.
2. R. W. Carlson *et al.*, in *Proceedings of the 7th International Kimberlite Conference*, J. J. Gurney, J. L. Gurney, M. D. Pascoe, S. H. Richardson, Eds. (Red Roof Design, Cape Town, 1999), pp. 99–108.
3. T. H. Jordan, *Rev. Geophys. Space Phys.* **13**, 1 (1975).
4. F. R. Boyd, *Earth Planet. Sci. Lett.* **96**, 15 (1989).
5. H. Helmstaedt, D. J. Schulze, *Geol. Soc. Aust.* **14**, 358 (1989).
6. S. H. Richardson, J. J. Gurney, A. J. Erlank, J. W. Harris, *Nature* **310**, 198 (1984).
7. M. J. de Wit *et al.*, *Nature* **357**, 553 (1992).
8. R. J. Hart, M. A. G. Andreoli, M. Tredoux, M. J. de Wit, *Chem. Geol.* **82**, 21 (1990).
9. A. A. Nyblade, in *Composition, Deep Structure and Evolution of Continents*, R. D. van der Hilst, W. F. McDonough, Eds., *Lithos* **48** (Scientific Publishers, Amsterdam, 1999), pp. 81–91.
10. M. Tredoux, R. J. Hart, R. W. Carlson, S. B. Shirey, *Geology* **27**, 923 (1999).
11. D. E. Moser, *Geology* **25**, 7 (1997).
12. A. M. Therriault, R. A. F. Grieve, W. U. Reimold, *Meteoritics* **32**, 71 (1997).
13. R. L. Gibson, G. Stevens, *Geol. Soc. London Spec. Publ.* **138** (1998), pp. 121–135.
14. D. Stepto, *Tectonophysics* **171**, 75 (1990).
15. R. J. Hart, H. J. Welke, L. O. Nicolaysen, *J. Geophys. Res.* **86**, 10663 (1981).
16. R. J. Hart, D. E. Moser, M. Andreoli, *Geology* **27**, 1091 (1999).
17. R. M. Flowers, thesis, University of Utah (2000).
18. D. W. Davis, *Can. J. Earth Sci.* **11**, 2141 (1982).
19. K. R. Ludwig, U.S. Geol. Surv. Open-File Rep. 91-0445, (1991).
20. J. B. Dawson, S. L. Harley, R. L. Rudnick, T. R. Ireland, *J. Metamorph. Geol.* **15**, 253 (1997).
21. L. J. Robb, D. W. Davis, S. L. Kamo, F. M. Meyer, *Nature* **357**, 677 (1992).
22. D. E. Moser, L. M. Heaman, T. E. Krogh, J. A. Hanes, *Tectonics* **15**, 1093 (1996).
23. L. Royden, *J. Geophys. Res.* **101**, 17679 (1996).
24. D. E. Moser, R. J. Hart, in *Proceedings of the 7th International Kimberlite Conference*, Cape Town, 13 to 17 April 1998 (Univ. of Cape Town, Cape Town, 1998), pp. 609–611.
25. M. Schmitz, S. Bowring, *Chem. Geol.*, **172**, 59 (2001).
26. S. B. Shirey *et al.*, *Geophys. Res. Lett.*, in press.
27. S. H. Richardson, S. B. Shirey, J. W. Harris, R. W. Carlson, in preparation.
28. D. G. Pearson, H. O. A. Meyer, F. R. Boyd, S. B. Shirey, R. W. Carlson, in *Proceedings of the 6th International Kimberlite Conference*, Novosibirsk, 7 to 13 August 1995 (Russian Academy of Science, Siberia, 1995), pp. 427–429.
29. D. Jacob, E. Jagoutz, D. Lowry, D. Mattey, G. Kudrjavt-seva, *Geochim. Cosmochim. Acta* **58**, 5191 (1994).
30. J. S. Stacey and J. D. Kramers, *Earth Planet. Sci. Lett.* **26**, 207 (1975).
31. Supported by NSF grant no. EAR9805210. Resources for U-Pb dating (Royal Ontario Museum) and initial logistical support from M.J. de Wit (University of Cape Town) are gratefully acknowledged, as are discussions with our U.S. and African collegues in the Kaapvaal Craton Project.

Sound Velocities in Iron to 110 Gigapascals

Guillaume Fiquet,[1]* James Badro,[1] François Guyot,[1] Herwig Requardt,[2] Michael Krisch[2]

The dispersion of longitudinal acoustic phonons was measured by inelastic x-ray scattering in the hexagonal closed-packed (hcp) structure of iron from 19 to 110 gigapascals. Phonon dispersion curves were recorded on polycrystalline iron compressed in a diamond anvil cell, revealing an increase of the longitudinal wave velocity (V_P) from 7000 to 8800 meters per second. We show that hcp iron follows a Birch law for V_P, which is used to extrapolate velocities to inner core conditions. Extrapolated longitudinal acoustic wave velocities compared with seismic data suggest an inner core that is 4 to 5% lighter than hcp iron.

The knowledge of the elastic constants of the phases of iron, which makes up 70 to 90 weight % of planetary cores, is essential for comparison with global velocity models of Earth. The hcp (or ε) high-pressure phase of iron is stable to at least 300 GPa at ambient temperature (1). Elastic properties of hcp iron have been determined to 210 GPa by x-ray diffraction (XRD) lattice strains measurements (2, 3), but these results show discrepancies with calculations using first-principles methods (4-7), as well as with a recent experimental investigation to 42 GPa by nuclear resonant inelastic x-ray scattering (NRIXS) of synchrotron radiation (8). The most recent investigation with NRIXS (9), however, yielded results consistent with lattice strain measurements (3). Elastic properties of hcp iron determined by Raman spectroscopy to 156 GPa yielded a C_{44} elastic modulus that is lower than previous determinations (10). Inconsistencies among these studies might be partly attributed to the fact that none of these techniques directly measures the acoustic wave velocities of iron. This limitation can be overcome by inelastic x-ray scattering (IXS) with meV energy resolution, where the acoustic velocity can be directly derived from the dispersion of the acoustic phonon energy (11, 12).

Our IXS experiment was carried out at the inelastic scattering beamline ID28 at the European Synchrotron Radiation Facility

[1]Laboratoire de Minéralogie et Cristallographie, UMR CNRS 7590, Université Paris VI, 4 Place Jussieu, 75252 Paris cedex 06, France. [2]European Synchrotron Radiation Facility, BP220, 38043 Grenoble cedex, France.

*To whom correspondence should be addressed. E-mail: fiquet@lmcp.jussieu.fr

(ESRF) in Grenoble, France. The undulator x-ray beam was monochromatized by a cryogenically cooled silicon (111) crystal and by a very high energy resolution monochromator, operating in backscattering geometry and using the silicon (888) reflection order. This beam, with an energy of 15.618 keV and an energy resolution of 3.9 meV, was focused with a gold-coated mirror down to a beam size of 270 μm by 80 μm (horizontal by vertical, full width at half maximum) at the sample location. These incident beam dimensions were further reduced by slits to avoid scattering from the high-pressure cell gasket. The scattered photons were collected by five spherical silicon crystal analyzers operating in backscattering and Rowland circle geometry at the same reflection order as the high-resolution monochromator. The momentum transfer Q [$Q = 2k_0 \sin(\theta_S/2)$, where k_0 and θ_S are the wave vector of the incident photon and the scattering angle, respectively] was selected by rotating the 7-m-long spectrometer arm in the horizontal plane. Spectra were collected simultaneously at five different momentum transfers [$Q = 4, 6.16, 8.31, 10.46,$ and 12.62 nm^{-1}]. A powdered iron sample (99.999% purity) was loaded into the 120-μm hole of a rhenium gasket and compressed between diamond anvils. Pressures were determined with the ruby fluorescence technique (13) and cross-checked by XRD (14). The maximum pressure of 112 GPa determined according to the isothermal equation of state of iron (1) agrees well with the ruby fluorescence method, which yielded 110 GPa. The experiment was performed on a polycrystalline sample of iron because it is impossible to preserve a single crystal while crossing the phase boundary from the low-pressure body-centered cubic structure (bcc, or α phase) to the hcp structure between 12 and 15 GPa (15). Data have been collected at three pressures (ambient pressure, 0.2 GPa, and 7 GPa) on the bcc structure of iron and at six pressures (19, 28, 45, 55, 64, and 110 GPa) on the hcp structure.

A typical IXS spectrum and its corresponding fits are shown as a function of transfer energy in Fig. 1. The peak centered at zero-energy transfer corresponds to the elastic contribution to the signal, whereas two other peaks are visible at higher energy transfer. The knowledge of the phonon dispersion curves of iron (16) and diamond (17) at ambient pressure allows an unambiguous assignment of these features. The inelastic signal at high-energy transfer (i.e., high acoustic wave velocity) corresponds to the transverse acoustic (TA) phonon branch of the diamond anvils, whereas the remaining peak is attributed to the longitudinal acoustic (LA) phonon of iron. These inelastic contributions shift toward higher energies with increasing Q values (Fig. 2), so that the inelastic contribution from diamond moves out of the energy transfer window at $Q > 4$ nm^{-1}. At 8.31 and 10.46 nm^{-1}, an additional feature is visible between the quasi-elastic line and the LA phonon of iron. Wave velocities derived from the energy position of these excitations suggest that they correspond to the TA phonon of iron. The TA phonons, however, were detected at two momentum transfers and at two pressures only, precluding any further attempt to derive the pressure dependence of the shear velocities of iron. At variance, the LA phonon branch is observed over the entire momentum and pressure range explored.

Table 1. Acoustic sound velocities of hcp and bcc iron at 298 K and high pressures.

P (GPa)	V_P (km s^{-1})
0.2	5.91 ± 0.06*
7 ± 0.1	6.30 ± 0.06*
19 ± 0.3	7.06 ± 0.10
28 ± 0.5	7.36 ± 0.18
45 ± 0.9	7.80 ± 0.20
55 ± 1.2	8.03 ± 0.24
64 ± 1.5	8.22 ± 0.25
110 ± 2	8.80 ± 0.44

*Recorded on the bcc phase of iron.

The LA wave velocity V_P was determined at each pressure by fitting the dispersion curve with a sine function

$$E \text{ [meV]} = 4.192 \times 10^{-4} \, V_P \text{ [m/s]}$$
$$\times \, Q_{MAX} \text{ [nm}^{-1}\text{]} \sin\left[\frac{\pi}{2} \frac{Q \text{ [nm}^{-1}\text{]}}{Q_{MAX} \text{ [nm}^{-1}\text{]}}\right] \quad (1)$$

from which V_P as well as the position of the edge of the first Brillouin zone, Q_{MAX}, can be derived (Fig. 3). Data recorded at four to five momentum transfers have been used in each dispersion curve to constrain V_P within an estimated error of 3%, with the exception of the data point at 110 GPa, for which only two momentum transfer data points could be used. The observed values of Q_{MAX} are in agreement with those calculated after (1). At 110 GPa, the acoustic wave velocity was determined with a fixed Q_{MAX} calculated after (1). LA wave velocities as a function of
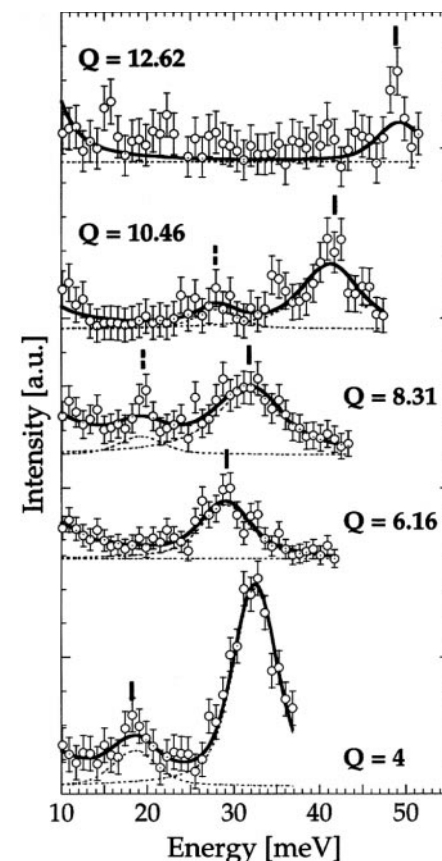
Fig. 2. Dispersion of the iron LA phonon with increasing Q values (in nm^{-1}). LA phonons of iron are indicated by ticks. A TA mode detected at $Q = 8.31$ nm^{-1} and at $Q = 10.46$ nm^{-1} is indicated by broken ticks. Data are normalized to the intensity of the iron LA phonon peak. The integration time for each point was of the order of 600 to 700 s, obtained by a summation of four to six scans in the range of 0 to 50 meV. The energy position of the phonons could be determined with a relative error of typically 3%. Error bars indicate the estimated SD of the photon-counting process. a.u., arbitrary units.
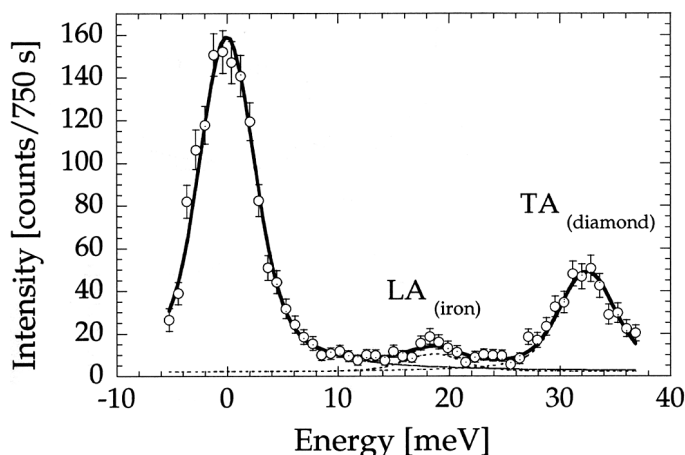

Fig. 1. IXS spectra of hcp iron at 28 GPa and the Q value of 4 nm^{-1}. The experimental data (open circles) are plotted along with corresponding fits. The energy positions and the widths of the excitations were fitted by using a Lorentzian model function, convoluted with the experimentally determined energy resolution function, by standard χ^2 minimization. Dashed lines represent the inelastic contributions of the LA phonon branch for iron and from a TA branch of the diamond anvil. The thin solid line represents the elastic contribution and the thick continuous line shows the summation of individual contributions. Error bars indicate the estimated SD of the photon-counting process.

pressure are summarized in Table 1. Our results for the low-pressure bcc structure agree with the ultrasonic data collected to 1 GPa (18) and extrapolated to 10 GPa within 1%, thus attesting to the reliability of these measurements (19).

Our results for the high-pressure hcp structure of iron (Fig. 4) compared with shock wave measurements (20) show that hcp iron follows a Birch law (21) for V_P, which provides a convenient relation for extrapolating our measurements to higher pressures. Seismic data (22) do not fit the experimental extrapolation, suggesting that Earth's inner core is slightly lighter than hcp iron, as proposed in earlier work (1, 23). The density differences are 4 to 5%.

Our measurements are consistent with the ultrasonic data (3), the XRD measurements (3), and the NRIXS data (9) below 100 GPa (Fig. 5). Above 100 GPa, however, our extrapolation departs from these measurements, yielding lower acoustic velocities than those derived from XRD (3) and NRIXS experiments (9). In the same manner, one observes a substantial dis-crepancy with results from theoretical calculations (4–7) at pressures of 210 GPa.

Our IXS experiment on a polycrystalline iron sample only allows us to determine the orientationally averaged dispersion curves for the LA phonon branch. The experiment is therefore sensitive to preferred orientations of crystals in the sample, when reciprocal lattice vectors are not randomly oriented in comparison with Q. XRD measurements carried out in parallel to our IXS study (14) indicate randomly oriented iron crystals at pressures below 40 GPa. At low pressure, we find an excellent agreement between our V_P measurements and orientationally averaged ultrasonic data (3). At pressures higher than 50 GPa, our diffraction data show that hcp iron displays a concentration of c axes parallel to the diamond anvil cell compression axis, in agreement with recent XRD texture measurements (24). Those XRD measurements (24) predict a large anisotropy for V_P, with P waves traveling 18% faster at 45° from the c axis than either in the ab plane or along the c axis. According to our XRD measurements, the x-ray inelastic scattering by acoustic phonons is made preferentially in the ab plane, because momentum transfer lies perpendicular to the incident x-ray beam and to the c axis. Consequently, one could have underestimated V_P as preferred orientations develop. When anisotropy curves are considered (3, 24), however, the orientationally averaged values of V_P are similar, within a few percent, to the values corresponding to a predominant but not complete preferential orientation of the c axis [figure 4 in (3)]. Taking into account experimental error bars, the values of V_P measured in this study should therefore be indistinguishable from orientationally averaged values. Up to 100 GPa, the agreement with measurements of V_P by XRD data (3) is good (Fig. 5), suggesting that the isostress assumption used for interpreting such data, experimentally validated for cubic phases of iron and iron oxide only (2), might be valid for hcp iron as well. A direct comparison with NRIXS data (8, 9) is more difficult. In such experiments, the strong elastic line has to be subtracted in order to perform a meaningful parabolic fit of the low-energy part of the density of states. This yields an average Debye phonon velocity, which has to be converted into V_P and shear wave velocity V_S through an a priori averaging scheme. We note, however, that our V_P measurements are encouragingly consistent with V_P values derived from vibrational densities of state measured by NRIXS (9), although extrapolation of the trends outside of the actual measurement ranges would yield very different values of V_P at inner core conditions.

Fig. 3. LA phonon dispersion curves of iron at different pressures. Lines represent the results of the fit of Eq. 1. Solid symbols and dashed lines stand for measurements carried out on the bcc phase at 0.2 and 7 GPa. Open symbols and solid lines correspond to the pattern recorded on the hcp structure of iron at 19, 28, 45, 55, 64, and 110 GPa from bottom to top, respectively. The energy position of the phonons could be determined within 3% (error bars).
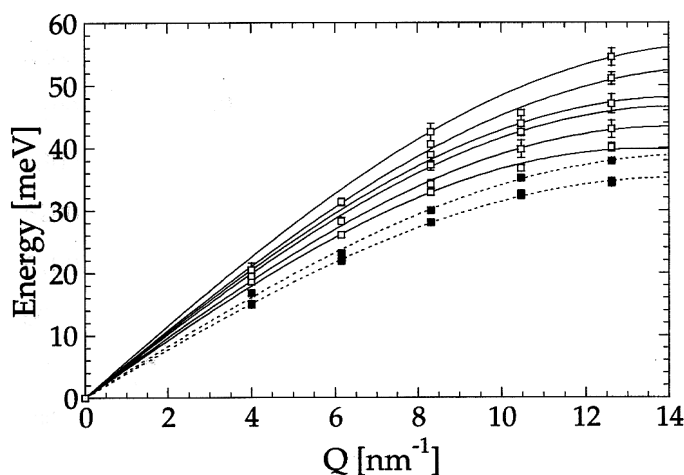

Fig. 4. LA wave velocities of hcp iron [open squares (this work)] and solid diamonds [shock wave Hugoniot measurements (20)] as a function of specific mass. Preliminary Reference Earth Model seismic data are represented by open diamonds (22). As shown by the dashed line, the experimental points for pure iron move along a straight line. This linear relation between velocity and density, known as Birch's law, is described in detail in (21). Error bars indicate the error in V_P as obtained from Eq. 1.
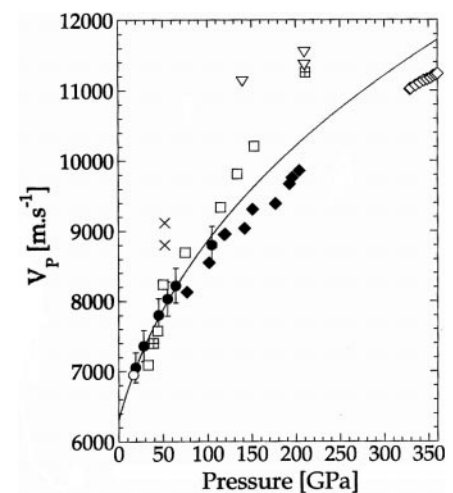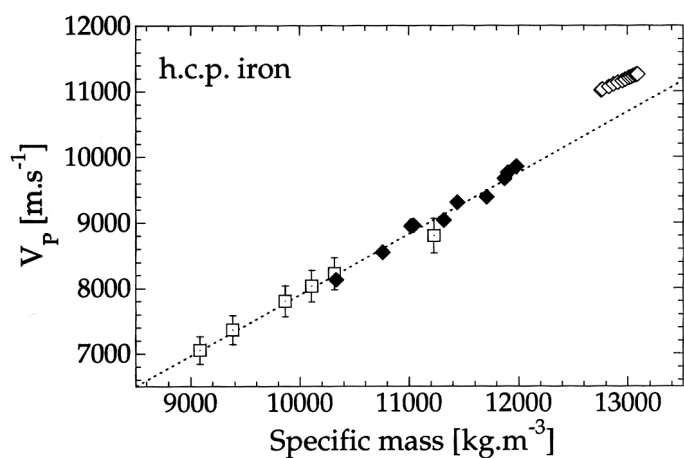

Fig. 5. LA wave velocities (V_P) of iron as a function of pressure for the present work (●) and extrapolated at higher pressure after a Birch fit to our data (solid line) and plotted along with ultrasonic (○) and XRD measurements (⊞) (3), XRD measurements (×) (2), NRIXS data (□) (9), shock wave Hugoniot measurements not reduced to 300 K (◆) (20), observations for the inner core (◇) (22), and ab initio calculations (▽) (4–7). The possible effects of preferred orientations as estimated from (3) and (24) are within the displayed error bars.

References and Notes

1. H. K. Mao, Y. Wu, L. C. Chen, J. Shu, A. P. Jephcoat, *J. Geophys. Res.* **95**, 21737 (1990).
2. A. K. Singh, H. K. Mao, J. Shu, R. J. Hemley, *Phys. Rev. Lett.* **80**, 2157 (1998).
3. H. K. Mao *et al.*, *Nature* **396**, 741 (1998); *Nature* **399** (correction), 280 (1999).
4. L. Stixrude, R. E. Cohen, *Science* **267**, 1972 (1995).
5. P. Söderlind, J. A. Moriarty, J. M. Wills, *Phys. Rev. B* **53**, 14063 (1996).
6. G. Steinle-Neumann, L. Stixrude, R. E. Cohen, *Phys. Rev. B* **60**, 791 (1999).
7. A. Laio, S. Bernard, G. L. Chiarotti, S. Scandolo, E. Tosatti, *Science* **287**, 1027 (2000).
8. R. Lübbers, H. F. Grünsteudel, A. I. Chumakov, G. Wortmann, *Science* **287**, 1250 (2000).
9. H. K. Mao *et al.*, personal communication.
10. S. Merkel, A. F. Goncharov, H. Mao, P. Gillet, R. J. Hemley, *Science* **288**, 1626 (2000).
11. E. Burkel, *Inelastic Scattering of X-rays with Very High Energy Resolution* (Springer, New York, 1991).
12. G. Ruocco *et al.*, *Nature* **379**, 521 (1996); M. Krisch *et al.*, *Phys. Rev. B* **56**, 8691 (1997).
13. H. K. Mao, P. M. Bell, J. W. Shaner, D. J. Steinberg, *J. Appl. Phys.* **49**, 3276 (1978).
14. Angle-dispersive XRD experiments were carried out at the ID30 high-pressure beamline at a wavelength of 0.3738 Å. Patterns were collected on imaging plates located 350 mm from the sample. The x-ray beam size at the sample location was 10 μm by 15 μm.
15. N. Von Bargen, R. Boehler, *High Pressure Res.* **6**, 133 (1990).
16. V. J. Minkiewicz, G. Shirane, R. Nathans, *Phys. Rev.* **162**, 528 (1967).
17. J. L. Warren, J. L. Yarnell, G. Dolling, R. A. Cowley, *Phys. Rev.* **158**, 805 (1967).
18. M. W. Guinan, D. N. Beshers, *J. Phys. Chem. Solids* **29**, 541 (1968).
19. Web fig. 1 is available at www.sciencemag.org/cgi/content/full/291/5503/468/DC1/.
20. J. M. Brown, R. G. McQueen, *J. Geophys. Res.* **91**, 7485 (1986).
21. F. Birch, in *Solids Under Pressure*, W. Paul, D. M. Warschauer, Eds. (McGraw-Hill, New York, 1963), pp. 137–162; *Geophys. J. R. Astron. Soc.* **4**, 295 (1961).
22. A. M. Dziewonski, D. L. Anderson, *Phys. Earth Planet. Inter.* **25**, 297 (1981).
23. A. P. Jephcoat, P. Olson, *Nature* **325**, 332 (1987).
24. H. R. Wenk, S. Matthies, R. J. Hemley, H. K. Mao, J. Shu, *Nature* **405**, 1044 (2000).
25. We thank S. Merkel, H. R. Wenk, and H. K. Mao for communicating unpublished results and B. Couzinet and J. C. Chervin for their help in the preparation of the samples and high-pressure cells. M. Mezouar is warmly acknowledged for his help during the unscheduled XRD experiments carried out at the ID30 beam station (at ESRF). Contribution CNRS-INSU IT 257.

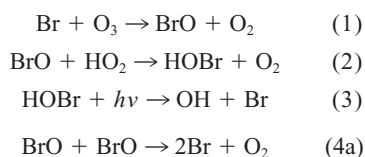# The Role of Br₂ and BrCl in Surface Ozone Destruction at Polar Sunrise

Krishna L. Foster,[1] Robert A. Plastridge,[2] Jan W. Bottenheim,[3] Paul B. Shepson,[4] Barbara J. Finlayson-Pitts,[1] Chester W. Spicer[2]*

Bromine atoms are believed to play a central role in the depletion of surface-level ozone in the Arctic at polar sunrise. Br₂, BrCl, and HOBr have been hypothesized as bromine atom precursors, and there is evidence for chlorine atom precursors as well, but these species have not been measured directly. We report here measurements of Br₂, BrCl, and Cl₂ made using atmospheric pressure chemical ionization–mass spectrometry at Alert, Nunavut, Canada. In addition to Br₂ at mixing ratios up to ~25 parts per trillion, BrCl was found at levels as high as ~35 parts per trillion. Molecular chlorine was not observed, implying that BrCl is the dominant source of chlorine atoms during polar sunrise, consistent with recent modeling studies. Similar formation of bromine compounds and tropospheric ozone destruction may also occur at mid-latitudes but may not be as apparent owing to more efficient mixing in the boundary layer.
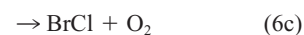
Surface-level O_3 depletion events, at times marked by O_3 mixing ratios below 1 part per billion (ppb) (nmol/mol air), have been observed at polar sunrise (March through May) throughout the Arctic for over a decade (*1–4*). This depletion has been shown to be correlated with Br associated with particles (*3, 5*), leading to the hypothesis that the O_3 depletion is caused by a chain reaction initiated by a Br atom (*3*). Laboratory kinetic experiments and mechanistic data suggest that the chain is initiated through the photolysis of gas phase Br compounds (*6–8*). The BrO free radical, a key intermediate in the Br-catalyzed destruction of O_3, has been observed at ground level over the Arctic (*9, 10*). Although the source of active Br is believed to be oxidation of Br^- in sea-salt aerosol, snow, and frozen ocean surfaces (*11, 12*), the mechanism is not well understood. The key to elucidating the chemistry leading to lower atmospheric ozone depletion in the Arctic, and possibly at mid-latitudes, is the measurement of specific gaseous halogen compounds present before and during ozone depletion episodes.

Ozone depletion by gas phase Br reactions occurs via reactions 1 to 5:

$$Br + O_3 \rightarrow BrO + O_2 \qquad (1)$$
$$BrO + HO_2 \rightarrow HOBr + O_2 \qquad (2)$$
$$HOBr + h\nu \rightarrow OH + Br \qquad (3)$$
$$BrO + BrO \rightarrow 2Br + O_2 \qquad (4a)$$
$$\rightarrow Br_2 + O_2 \qquad (4b)$$
$$Br_2 + h\nu \rightarrow 2Br \qquad (5)$$

Cross-reactions of BrO with ClO may also be important (*13*):

$$BrO + ClO \rightarrow Br + OClO \qquad (6a)$$
$$\rightarrow Br + ClOO \qquad (6b)$$
$$\rightarrow BrCl + O_2 \qquad (6c)$$
$$BrCl + h\nu \rightarrow Br + Cl \qquad (7)$$

Removal of Br atoms from the chain occurs through reactions with organic compounds such as formaldehyde, which are present in measurable concentrations in the polar spring at high Arctic sites (*14*). The Br^- ion in the product HBr is then temporarily sequestered in aerosol, surface snow, and ice.

To sustain the chain destruction of ozone, there must be heterogeneous reactions to activate Br^- ions from aerosol and surface snowpack into a gaseous photochemically active form. For example, the uptake of gaseous HOBr on snow followed by its reaction with Br^- was suggested as a recycling mechanism for Br₂ in the Arctic (*15*):

$$HOBr + H^+ + Br^- \xrightarrow[\text{ice}]{\substack{\text{aqueous} \\ \text{phase}}} Br_2 + H_2O \qquad (8)$$
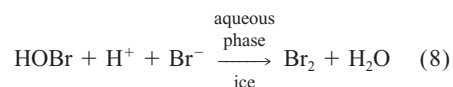
There is laboratory evidence for the production of Br₂ via reaction 8 [e.g., (*16, 17*)].

Previous measurements indicated the presence of a large source of photochemically active Br and Cl precursors (*6, 7*), but the technique used was nonspecific and therefore left proof for the presence of Br₂ and other halogen atom precursors open. Here we report results from specific measurements of Br₂, BrCl, and Cl₂ in the troposphere of the high Arctic, ~125 cm above the snow.

Figure 1 shows the mixing ratios of Br₂, BrCl, and O_3 between 9 February and 13 March 2000 (day of year 40 to 73) (*18*). BrCl was first observed above the 2-ppt detection limit on day 54 (23 February). The maximum Br₂ and BrCl

[1]Department of Chemistry, University of California, Irvine, CA 92697–2025, USA. [2]Battelle, 505 King Avenue, Columbus, OH 43201–2693, USA. [3]Environment Canada, 4905 Dufferin Street, Toronto, Ontario M3H 5T4, USA. [4]Department of Chemistry and Department of Earth and Atmospheric Sciences, Purdue University, West Lafayette, IN 47907–1393, USA.

*To whom correspondence should be addressed. E-mail: spicerc@battelle.org